



Multi-wavelength Study of HESS J1303-631 with 14 yr of Fermi-LAT Data

Lian-Cheng Zhou, Qi Xia, Shi-Ting Tian, Yun-Lu Gong, and Jun Fang
Department of Astronomy, Yunnan University, Kunming 650091, China; fangjun@ynu.edu.cn
Received 2023 April 4; revised 2023 July 16; accepted 2023 July 25; published 2023 September 19

Abstract

HESS J1303-631 is an extended TeV pulsar wind nebula powered by the pulsar PSR J1301-6305 detected with the High Energy Stereoscopic System. We present an analysis of the GeV γ -ray region of HESS J1303-631 with about 14 yr of Fermi Large Area Telescope data. The GeV γ -ray emission, coincident with the very-high-energy source, has a photon index of 1.69 ± 0.09 in 10–500 GeV band, and the GeV morphology has an extension to the same direction as indicated in the TeV band. Moreover, the observed multi-wavelength spectral energy distribution of the nebula is studied with a one-zone time-dependent leptonic model, in which the electrons/positrons injected into the nebula are assumed to have a broken power-law spectrum. The result indicates that the multi-wavelength non-thermal emission can be well reproduced via synchrotron radiation and inverse Compton scattering of the particles.

Key words: ISM: supernova remnants – radiation mechanisms: non-thermal – ISM: general

1. Introduction

Driven by energetic pulsars, pulsar wind nebulae (PWNe) are the predominant class of very high energy (VHE) (≥ 100 GeV) γ -ray sources and multi-wavelength emitters in the Galaxy (Reynolds et al. 2017). Some PWNe have been detected as non-thermal emission sources between ~ 100 MHz (Driessen et al. 2018) and extremely high energy γ -rays ($\sim 10^{15}$ eV) (Lhaaso Collaboration et al. 2021). A significant fraction (~ 40) of the Galactic TeV sources are related to PWNe,¹ and high-energy γ -ray detection helps us to understand the physical mechanisms that produce these energetic particles in PWNe and the origin of Galactic cosmic rays (CRs) (Fang et al. 2020; de Oña Wilhelmi et al. 2022). The spectral energy distribution (SED) of PWNe can be characterized by a double-hump structure, i.e., a low-energy hump and a high-energy one produced by synchrotron and inverse Compton scattering off the background soft photons, respectively. The background soft photon field contains the synchrotron photons, cosmic microwave background (CMB) and infrared (IR)/optical photon fields (Tanaka & Takahara 2010; Torres et al. 2014).

HESS J1303-631, one of the Galactic VHE γ -ray sources, was discovered by Aharonian et al. (2005). Initially, there was no counterpart associated with it in other bands, and it was referred to as a so-called “dark source” since its nature was unclear. Until 2012, High Energy Stereoscopic System (H.E.S.S.) conducted an elaborate analysis of the morphology of HESS J1303-631, taking into consideration its dependence on energy, and it was argued that HESS J1303-631 should be an ancient PWN powered by PSR J1301-6305. The pulsar has a spin-down power of $\dot{E} = 1.70 \times 10^{36}$ erg s⁻¹ (Manchester et al. 2005) and a

characteristic age of 11 kyr. Moreover, H.E.S.S. Collaboration et al. (2012) presented the detection of a very faint X-ray PWN with XMM-Newton, the size of which extended $2' \sim 3'$ from the position of the pulsar to the center of the VHE γ -ray emission region. The tail-like extension of the X-ray source provided a hint as to the birthplace of the pulsar, later considered to be supernova remnant (SNR) G304.4-0.2 by radio detection (Sushch et al. 2017), which could lead to PSR J1301-6305 becoming the fastest known pulsar (~ 3100 km s⁻¹). However, there was no significant radio emission detected corresponding to HESS J1303-631 (Sushch et al. 2017).

GeV γ -rays from HESS J1303-631 have been detected by the Fermi Large Area Telescope (Fermi-LAT). Acero et al. (2013) analyzed 45 months of LAT data in the range of 10–316 GeV and presented the morphology of a Gaussian with a dispersion of $0^\circ.45$ and a spectral index of ~ 1.7 . In this work, we have carried out the morphological analysis and spectral analysis of HESS J1303-631 with 14 yr of Fermi-LAT data and obtained a different extension $R_{68} = 0^\circ.32 \pm 0^\circ.04$ under the Gaussian template with a spectral index of 1.69 ± 0.09 in the 10–500 GeV band. The defined radius does not include Kes 17 or other Fermi sources, which can more accurately describe the GeV γ -ray radiation. The multi-wavelength SED of HESS J1303-631 was initially modeled with a stationary leptonic model (H.E.S.S. Collaboration et al. 2012) and more recently studied by the time-dependent leptonic model with previous data (Zhu et al. 2018; Joshi et al. 2023). Here, we adopt a one-zone time-dependent leptonic model to investigate the radiative properties of HESS J1303-631. In this model, the PWN powered by PSR J1301-6305 can produce the multi-wavelength emission. Thanks to the multi-band observations and

¹ <http://tevcat.uchicago.edu/>

updated Fermi-LAT data results, the parameters of the model are better constrained.

In this paper, Section 2 presents the particulars of the data analysis. Section 3 describes the model of the SED of PWNe. Section 4 provides the results and discussion. Finally, Section 5 features a summary of the findings presented in this paper.

2. Fermi-LAT Data Analysis

2.1. Data Reduction

We carry out a binned likelihood analysis of GeV emission toward HESS J1303-631 by the available software `Fermipy` (Wood et al. 2021). We adopt the instrumental response function `P8R3_SOURCE_V3` with the latest data from Pass 8, using “Source” class (`evclass = 128`) and “FRONT+BACK” type events, collected from 2008 August 4 to 2022 June 10 (Fermi mission elapsed time 239557417–676515024 s). In addition, the standard filtering options “(DATA_QUAL > 0) &&(LAT_CONFIG==1)” are used to identify a good time interval for our analysis. Meanwhile, the maximum zenith angle is fixed to 90° to limit contamination of γ -rays from the Earth’s limb. We selected a region of interest (ROI) with dimensions of $10^\circ \times 10^\circ$ centered on the target position (R.A. = $195^\circ 75'$, decl. = $-63^\circ 20'$) of 4FGL J1303.0-6312e, which is the Fermi GeV source counterpart to HESS J1303-631 (Abdollahi et al. 2020).

Our background model incorporates all sources within the ROI that are listed in the Fermi-LAT Fourth Source Catalog (4FGL; Abdollahi et al. 2020), as well as the isotropic γ -ray background emission (`iso_P8R3_SOURCE_V3_v1`) and the diffuse Galactic interstellar emission (`gll_iem_v07`). Subsequent analysis leaves the normalization and spectral parameters of the sources within 3° free in the background model. The normalization parameters of the isotropic and Galactic components are also left free.

2.2. Morphological Analysis

A test statistic (TS) map was created to examine the energy-dependent morphology of the GeV emission from HESS J1303-631. The TS value is given by $TS = 2(\ln \mathcal{L}_1 - \ln \mathcal{L}_0)$, in which $\ln \mathcal{L}_0$ is the background likelihood with $\ln \mathcal{L}_1$ being the likelihood of adding a hypothetical source. The excess map is created by background fitting only, excluding 4FGL J1303.0-6312e in the 10–500 GeV energy band. Then the significant GeV excess emission near HESS J1303-631 with spatial correlation to TeV radiation can be seen in the top right panel of Figure 1.

We tried different morphological models fitting the GeV excess emission in the 10–500 GeV band to select the best available representation. For convenience, we marked the significant GeV emission region as SrcX, and it was included in our model as a point source with a power-law spectrum to

enable likelihood analysis. Then, we calculated the best-fit position (R.A., decl. = $195^\circ 80'$, $-63^\circ 16'$, with 1σ error radius of $0^\circ 02'$) of SrcX by `gtfindsrc` according to the position of 4FGL J1303.0-6312e (R.A. = $195^\circ 75'$, decl. = $-63^\circ 20'$) (4FGL; Abdollahi et al. 2020). The TS value of the point source SrcX is 130.41, yielding a significance level of 10.83σ .

Furthermore, we examined the spatial distribution of γ -ray emission with a two-dimensional (2D) Gaussian model and a uniform disk model; the results of the best-fit analysis are presented in Figure 2. The 68% containment radius (with a 1σ statistical uncertainty) of SrcX in the uniform disk model is $R_{68} = 0^\circ 28' \pm 0^\circ 02'$ with a $TS_{\text{ext}} = 91.46$ and in the 2D Gaussian model is $R_{68} = 0^\circ 32' \pm 0^\circ 04'$ with a $TS_{\text{ext}} = 108.60$. The TS_{ext} is given by $TS_{\text{ext}} = 2(\ln \mathcal{L}_{\text{ext}} - \ln \mathcal{L}_{\text{ps}})$, in which $\ln \mathcal{L}_{\text{ext}}$ and $\ln \mathcal{L}_{\text{ps}}$ denote the maximum likelihood values obtained for the extended model and point-like model, respectively (Lande et al. 2012). Therefore, SrcX is defined as an extended source as $TS_{\text{ext}} \geq 16$ (a significance level of 4σ) (Lande et al. 2012).

In addition, we consider the Akaike information criterion (AIC; Akaike 1974), and the $\Delta AIC = AIC_{\text{point}} - AIC_{\text{ext}}$, where AIC_{point} and AIC_{ext} refer to the AIC values associated with a point source and an extended source, respectively. Then, we obtain $\Delta AIC = 89.43$ for the disk model and $\Delta AIC = 106.64$ for the Gaussian model. Therefore, we assume a 2D Gaussian template for SrcX and generate the residual map, as displayed in the bottom left panel of Figure 1, indicating no other significant residual γ -ray emission. Consequently, we have chosen SrcX to represent the GeV emission region of HESS J1303-631. The results of the spatial distribution analysis for SrcX are summarized in Table 1.

2.3. Spectral Analysis

In the vicinity of HESS J1303-631, Kes 17 (logged in 4FGL as 4FGL 1305.5-6241 4FGL; Abdollahi et al. 2020) is the nearest known SNR to PSR J1301-6305, which is $37'$ away in terms of angular distance (Wu et al. 2011). As affirmed in the top left panel of Figure 1, significant excess radiation with a TS value of ~ 101.73 from Kes 17 is evident. This is considered not to be a part of HESS J1303-631 due to the spatial offset of $\sim 0^\circ 58'$ from the peak radiation and no apparent continuous radiation being observed. The GeV emission region of SrcX does not include Kes 17 or other 4FGL γ -ray sources in our model. To further identify and verify that Kes 17 is a source independent of SrcX, we created its SED using a model of 4FGL J1305.5-6241 between the 10 and 500 GeV band, which is logged as a point source with a power-law index of ~ 2.36 in the 4FGL (Abdollahi et al. 2020). The spectrum of Kes 17 was fitted as a power-law with an index of ~ 2.12 , unlike the SrcX which has a harder spectral index of ~ 1.69 . These results are shown in Figure 4.

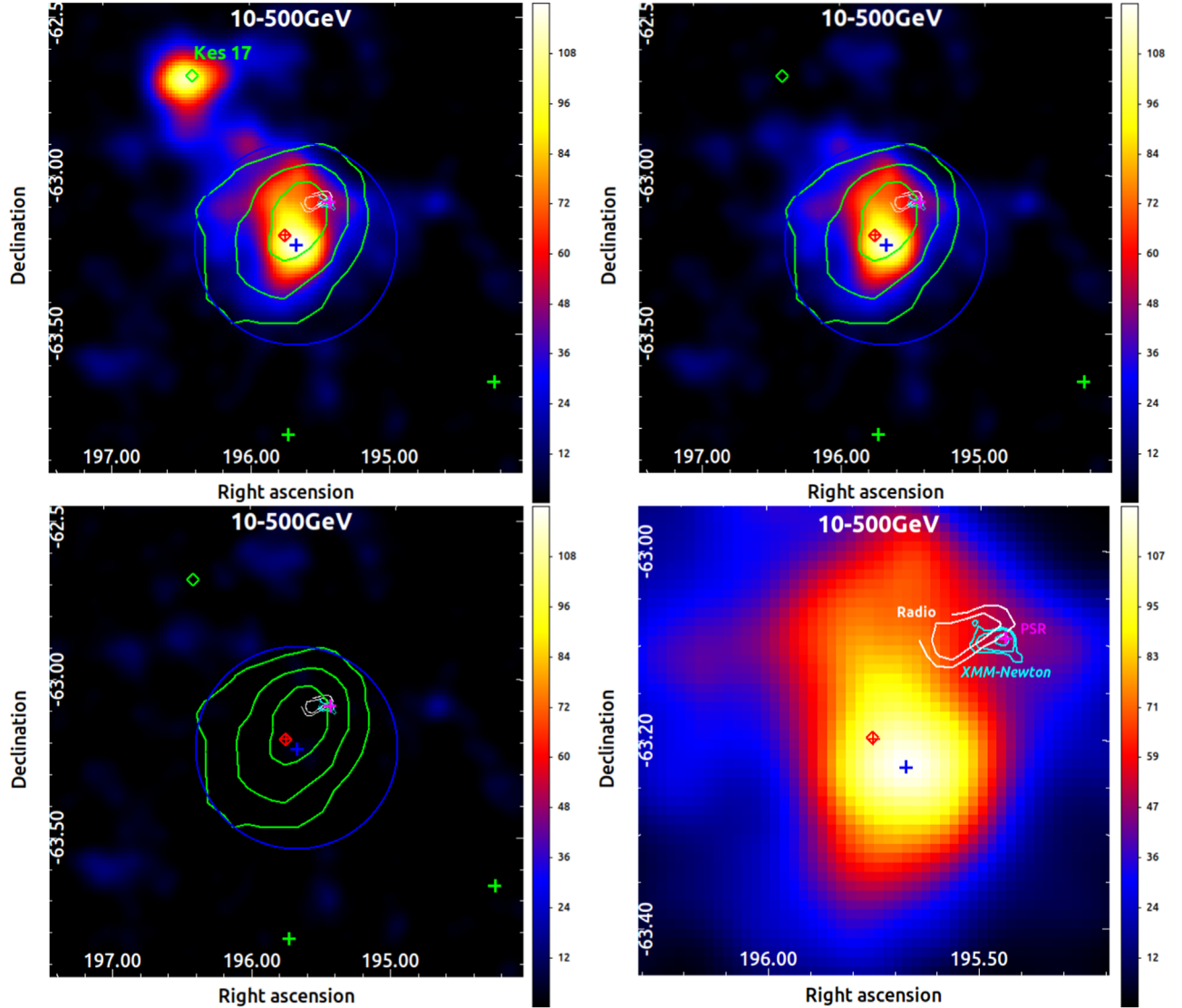


Figure 1. TS maps of the region centered at the position of 4FGL J1303.0-6312e marked as a red cross with $0''.01$ pixel size. The red diamond represents the position of HESS J1303-631 (Aharonian et al. 2005) and the blue cross signifies the best-fit position of SrcX. The magenta cross indicates the position of PSR J1301-6305, while the green, cyan and white contours correspond to H.E.S.S., XMM-Newton X-ray and radio observations (H.E.S.S. Collaboration et al. 2012), respectively. 4FGL sources are marked by green crosses, while Kes 17 is represented by a green square. The 68% containment region of the Gaussian source, used to model the GeV emission in this study, is depicted as a blue circle. The top left and top right panels display the excess maps wherein all background components (including 4FGL sources and diffuse backgrounds) have been subtracted, except for the top left panel retaining Kes 17. The bottom left panel shows the residual map with all sources removed. The bottom right panel is depicted in a $0''.4 \times 0''.4$ region in the 10–500 GeV band. Both maps were smoothed using a Gaussian function with a kernel radius of $0''.06$.

Based on the different spectral indices and spatial locations of SrcX and Kes 17 (R.A. = $196^\circ 39'$, decl. = $-62^\circ 69'$ for Kes 17), we consider Kes 17 to be independent of SrcX. Meanwhile, the hard spectral index of SrcX is also consistent with the spectral indices of the LAT-detected PWNe (Acero et al. 2013). Hence, HESS J1303-631 is considered to be the dominant source of contribution to GeV emission within this region in the 10–500 GeV energy band. Finally, the result of

the whole fit of the photon flux is $(4.39 \pm 0.41) \times 10^{-10}$ ph cm $^{-2}$ s $^{-1}$ with a spectral index of 1.69 ± 0.09 , and the SED of SrcX is depicted in Figure 4 and the specific values are shown in Table 2.

We focus on high-energy (>10 GeV) γ -ray events, for which the Fermi-LAT point-spread function offers better angular resolution. As for the events below 10 GeV, we have also performed an analysis. The excess map is also generated in the

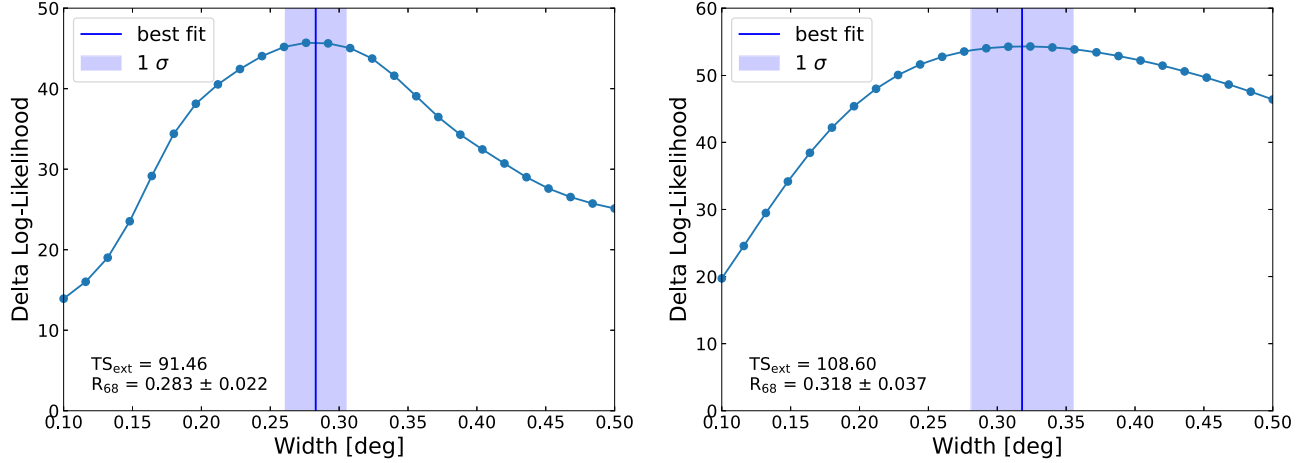


Figure 2. Extended likelihood curves for uniform disk model (left) and 2D Gaussian (right). The best-fit for the extension is represented by the blue vertical line, and the 1σ uncertainty is shown as a purple band.

Table 1
Spatial Distribution Analysis of SrcX using Different Models in the 10–500 GeV Energy Range

Model	Extension ($^{\circ}$)	Spectral Index	Photon Flux (10^{-10} ph cm $^{-2}$ s $^{-1}$)	TS Value	TS _{ext}	Δ AIC
Point source	...	1.63 ± 0.12	1.61 ± 0.24	130.41	...	106.64
Uniform disk	$0^{\circ}28 \pm 0^{\circ}02$	1.68 ± 0.09	3.73 ± 0.36	225.03	91.46	17.21
2D Gaussian	$0^{\circ}32 \pm 0^{\circ}04$	1.69 ± 0.09	4.39 ± 0.41	243.47	108.60	0

Note. The extension corresponds to their respective 68% containment radii for the disk and the Gaussian. The TS_{ext} corresponds to the extension significance of SrcX. The quantity referred to as Δ AIC is calculated as the difference between the AIC value for a given model and that of the model with the lowest AIC value, which in this case is the 2D Gaussian model. The 1σ uncertainties of the morphological and spectral parameters are presented.

Table 2
Evaluation of the Energy Flux of SrcX with Fermi-LAT Data in the 10–500 GeV Energy Band

E (GeV)	Band (GeV)	$E^2 dN/dE$ (10^{-12} erg cm $^{-2}$ s $^{-1}$)	TS
14.78	10–23.20	4.94 ± 0.88	73.82
32.33	23.20–50.00	8.77 ± 1.33	111.22
70.71	50.00–107.72	9.72 ± 1.90	73.44
154.63	107.72–232.08	8.34 ± 2.54	40.39
338.12	232.08–500.00	15.74 ± 4.78	50.59

100 MeV–10 GeV band by subtracting the background components. As confirmed in Figure 3, significant excess γ -ray emission extends toward the pulsar. The best-fit extension (shown in a blue circle) was fitted to be $R_{68} = 0^{\circ}34 \pm 0^{\circ}03$ with a TS value = 238.97 in the Gaussian template. Moreover, the SED was generated and is displayed in Figure 4. The spectral index of ~ 2.06 obtained in the 100 MeV–10 GeV band differs from the spectral index of ~ 1.69 between 10 and

500 GeV, implying a possible origin of a different radiation mechanism, which may come from the γ -ray emission of PSR J1301-6305. However, this source is found to have an extension of $\sim 0^{\circ}34$, and is at odds with the hypothesis. Such a low-energy band turnover, possibly associated with proton-proton interactions, suggests a hadronic nature of HESS J1303-631. A similar case may be MGRO J1908+06 (Li et al. 2021). In the region of HESS J1303-631, a plausible SNR radio shell with a radius of $\sim 12'$ centered at an angular distance of $19'$ from PSR J1301-6305 at distance ~ 1.5 kpc was reported (G304.4-0.2; Sushch et al. 2017), which is indicated by a cyan dashed circle in Figure 3. Using Mopra molecular line observations at 7 mm [CS(1–0), SiO(1–0, $\nu = 0$)], NANTEN CO(1–0) data and the Southern Galactic Plane Survey/GASS HI survey, several molecular clouds (MCs) were indeed identified in this region (Voisin et al. 2019). Moreover, Voisin et al. (2019) observed that the CO(1–0) emission overlaps with the location of the SNR candidate, which may highlight the presence of a putative molecular shell at distance ~ 1.5 kpc. The above-mentioned scenario supports a CR–MC interaction

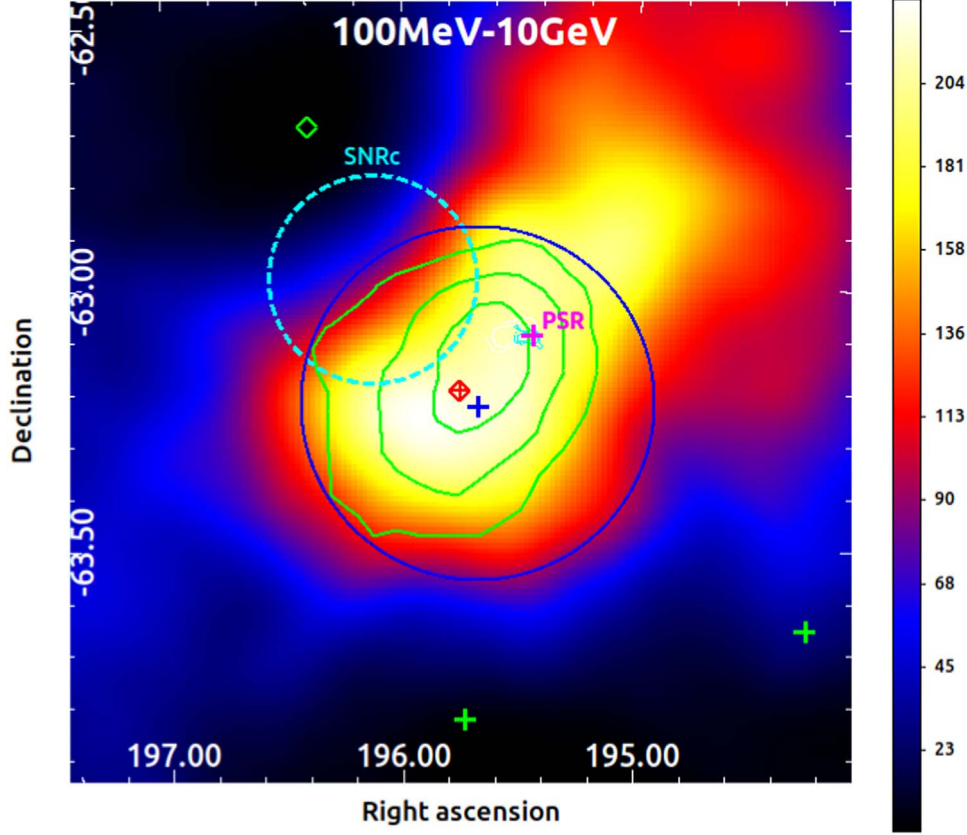


Figure 3. Excess map of the HESS J1303-631 region in the 0.1–10 GeV energy band with all background components removed. The best-fit extension (shown in a blue circle) was fitted to be ~ 0.34 in this energy band. The position and size of the SNR candidate from Sushch et al. (2017) is indicated by a cyan dashed circle. The remaining markings follow the same conventions as Figure 1.

at ~ 1.5 kpc as a possible origin for the lower-energy component of the emission. For PSR J1301-6305 at ~ 6.6 kpc (Cordes & Lazio 2002), we do not consider it to be physically associated with the SNR candidate, whereas it is associated with a PWN at ~ 6.6 kpc, which could contribute predominantly to the higher-energy part of the emission through inverse Compton scattering. Here, we adopt a one-zone time-dependent leptonic model to reproduce the multi-wavelength SED of HESS J1303-631, and we present our results below.

3. Brief Description of the Model

During the pulsar's spinning down, high-energy particles composed of electrons and positrons, which are accelerated by the termination shock, are continuously injected into the PWN around the pulsar. The energy spectrum of these high-energy particles is governed by (e.g., Martín et al. 2012)

$$\frac{\partial N(\gamma, t)}{\partial t} = -\frac{\partial}{\partial \gamma} [\dot{\gamma}(\gamma, t)N(\gamma, t)] - \frac{N(\gamma, t)}{\tau(\gamma, t)} + Q(\gamma, t), \quad (1)$$

in which the left-hand side represents how the distribution of the particles in terms of the Lorentz factor changes over time. On the right-hand side, $\dot{\gamma}(\gamma, t)$ is the summation of the energy losses due to adiabatic expansion, synchrotron radiation and inverse-Compton scattering. $\tau(\gamma, t)$ represents the amount of time it takes for high-energy leptons to escape the nebula via Bohm diffusion (Zhang et al. 2008). The parameter $Q(\gamma, t)$ describes the injection rate of particles per unit energy at a given time, which is commonly assumed to follow a broken power-law distribution, i.e.,

$$Q(\gamma, t) = Q_0(t) \begin{cases} \left(\frac{\gamma}{\gamma_b}\right)^{-\alpha_1} & \text{if } \gamma \leq \gamma_b \\ \left(\frac{\gamma}{\gamma_b}\right)^{-\alpha_2} & \text{if } \gamma_b < \gamma \leq \gamma_{\max}, \end{cases} \quad (2)$$

in which γ_b is the break Lorentz factor, and α_1 and α_2 are the spectral indices. $Q_0(t)$ is the normalization constant given by (Martín et al. 2012; Torres et al. 2014)

$$(1 - \eta)L(t) = \int \gamma m_e c^2 Q(\gamma, t) d\gamma, \quad (3)$$

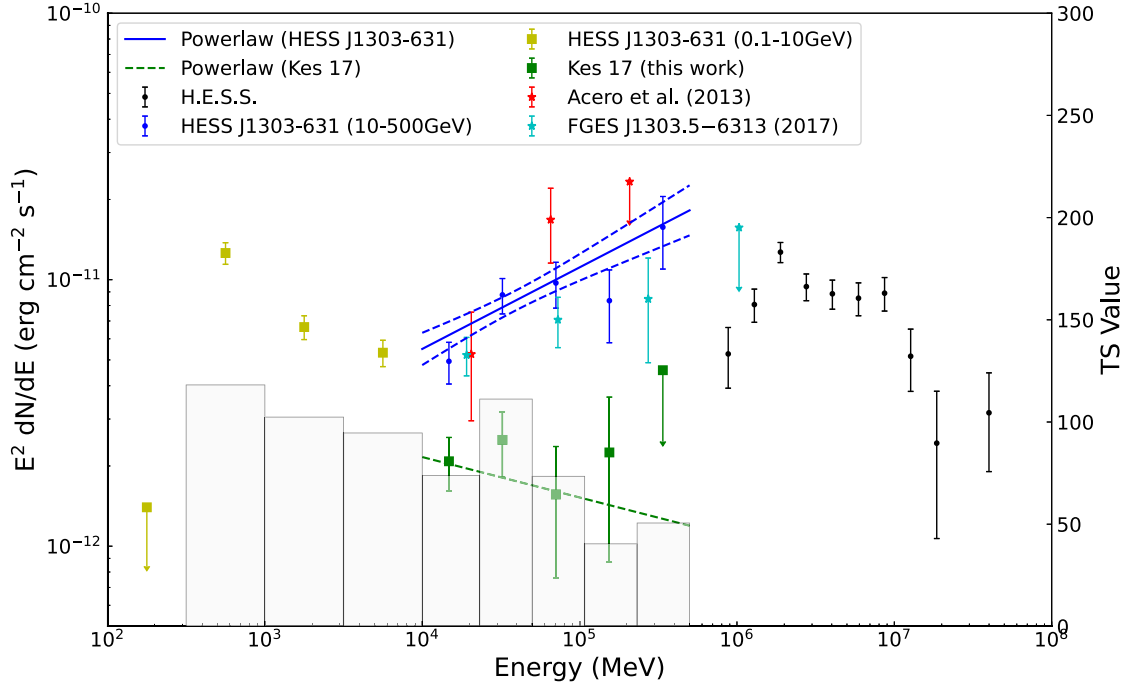


Figure 4. The SEDs of HESS J1303–631 and Kes 17, 95% upper limits are drawn when TS Value < 4. The yellow and blue dots with statistical uncertainties represent the results of the Fermi-LAT data analysis (in the 0.1–10 GeV and 10–500 GeV band, respectively), while the black dots mean the H.E.S.S. data (H.E.S.S. Collaboration et al. 2012). The best-fit spectrum and its 1σ statistical uncertainty for the blue dots are depicted, correspondingly, by the blue solid and dashed lines. For comparison, the SEDs obtained by previous work (Acero et al. 2013; Ackermann et al. 2017) are shown as the red and cyan star symbols, respectively. The gray-shaded region stands for the TS value in each energy bin of HESS J1303–631 obtained in this work. The green square symbols represent the SED of Kes 17 with the best-fit spectrum shown by the green dashed line.

where η represents the magnetic energy fraction and $L(t)$ denotes the injection luminosity (Gaensler & Slane 2006)

$$L(t) = L_0 \left(1 + \frac{t}{\tau_0} \right)^{-\frac{n+1}{n-1}}. \quad (4)$$

Here $L_0(t)$ is the initial luminosity, and $n = 2.5$ is the breaking index for PSR J1301-6305. In addition, the initial spin-down timescale of the pulsar is τ_0 which equals (Gaensler & Slane 2006)

$$\tau_0 = \frac{2\tau_c}{n-1} - t_{\text{age}}. \quad (5)$$

The characteristic age is $\tau_c = P/2\dot{P}$. The spin-down luminosity can be calculated with period P and period-derivative \dot{P} (Martín et al. 2012).

$$L(t) = 4\pi^2 I \frac{\dot{P}}{P^3}, \quad (6)$$

where $I = 10^{45} \text{ g cm}^2$ is moment of inertia of the pulsar. The spin-down power of a pulsar is converted into particle and magnetic energy, allowing for the calculation of the magnetic

field strength (Tanaka & Takahara 2010; Martín et al. 2012)

$$B(t) = \sqrt{\frac{3(n-1)\eta L_0 \tau_0}{R_{\text{PWN}}^3(t)} \left[1 - \left(1 + \frac{t}{\tau_0} \right)^{-\frac{2}{n-1}} \right]}, \quad (7)$$

where $R_{\text{PWN}}(t)$ is the radius of the nebula at time t . When the nebula has not encountered the reverse shock of the SNR, the radius of the nebula evolves as (van der Swaluw et al. 2001; van der Swaluw 2003; Torres et al. 2014)

$$R_{\text{PWN}}(t) = 0.84 \left(\frac{L_0 t}{E_0} \right)^{1/5} \left(\frac{10E_0}{3M_{\text{ej}}} \right)^{1/2} t. \quad (8)$$

Typical parameters, i.e., $E_0 = 10^{51} \text{ erg}$ and $M_{\text{ej}} = 9.5M_{\odot}$, are applied in this paper.

For the maximum energy of particles, the Larmor radius R_L plays a critical role, which should be less than a fraction of the radius of termination shock R_s . Specifically, the relation $R_L = \epsilon R_s$ follows, where ϵ represents the fractional size of the shock. Also, the maximum Lorentz factor can be obtained with

(Martín et al. 2012; Torres et al. 2014)

$$\gamma_{\max} = \frac{\epsilon e \kappa}{m_e c^2} \sqrt{\eta \frac{L(t)}{c}}, \quad (9)$$

where c is the speed of light, e is the electron charge, m_e is the mass of the electron and $\kappa=3$ represents the magnetic compression ratio (Holler et al. 2012; Martín et al. 2012).

4. Results and Discussion

As shown in Figure 1, the GeV emission region of HESS J1303-631 presents a large extension with the same extension direction as the TeV band. Moreover, we obtained that the best-fit extension of HESS J1303-631 is $R_{68} = 0^\circ.32 \pm 0^\circ.04$ with a TS value = 243.47 in the Gaussian template. The large size of HESS J1303-631 in the 10–500 GeV energy band suggests that a large number of high-energy electrons/positrons diffuse from the pulsar to great distances and interact with the surrounding environment to emit high-energy photons. Moreover, due to the high proper motion of the pulsar (Sushch et al. 2017), the centroid of the γ -ray emission is offset from PSR J1301-6305. The offset of the pulsar has also been observed in several other γ -ray PWNe, e.g., HESS J1640-465 (Xin et al. 2018), HESS J1825-137 (Principe et al. 2020) and HESS J1356-645 (Liu et al. 2023), all of which have extended GeV emission regions as well as hard GeV spectra.

HESS J1303-631 originates from the nebula powered by PSR J1301-6305 with a spin-down power $\dot{E} = 1.70 \times 10^{36} \text{ erg s}^{-1}$ (Manchester et al. 2005). Combining the results of our new Fermi analysis, we apply the one-zone time-dependent leptonic model to reproduce the SED for the PWNe powered by PSR J1301-6305. The rotation period and the first derivative period of the pulsar are 184 ms and $2.65 \times 10^{-13} \text{ s s}^{-1}$, respectively (Manchester et al. 2005; H.E.S.S. Collaboration et al. 2012), which result in a characteristic age of $\tau_c = 11,000 \text{ yr}$. The distance to PSR J1301-6305 was estimated to be 6.6 kpc (Cordes & Lazio 2002), and we adopted this distance here. Three components of the interstellar photon fields, i.e., CMB with temperature $T_{\text{cmb}} = 2.73 \text{ K}$ and an energy density of $U_{\text{cmb}} = 0.25 \text{ eV cm}^{-3}$, the IR background with $T_{\text{IR}} = 34 \text{ K}$ and $U_{\text{IR}} = 5.2 \text{ eV cm}^{-3}$ and starlight with $T_{\text{SL}} = 6700 \text{ K}$ and $U_{\text{SL}} = 10 \text{ eV cm}^{-3}$, are involved in the inverse Compton process to produce γ -rays from the PWNe. With the assumed age $t_{\text{age}} = 12,000 \text{ yr}$, the initial spin-down timescale is $\tau_0 = 2650 \text{ yr}$, and the initial spin-down luminosity is $L_0 = 9.09 \times 10^{37} \text{ erg s}^{-1}$. The magnetic field decreases with the expansion of the nebula with time, and we obtain the magnetic field strength $B = 2.6 \mu\text{G}$ with $\eta = 0.07$ and the radius of the nebula $R_{\text{PWN}} = 20.44 \text{ pc}$ at $t_{\text{age}} = 12,000 \text{ yr}$.

The Parkes-MIT-NRAO (PMN) survey at 4.85 GHz (Condon et al. 1993) detected a possible radio emission which was peaked about $3'$ east of the pulsar position. However, the significance was only 3σ for this emission, which was at the detection limit, therefore there were no definitive conclusions about its

morphology or flux in the radio band. The X-ray counterpart of the PWN was detected by XMM-Newton at $15''$ to the east of the position of the pulsar (H.E.S.S. Collaboration et al. 2012). The X-ray extension of the PWN powered by PSR J1301-6305 is rather smaller than that in the GeV γ -rays, and the X-rays are concentrated on the pulsar. In our model, the X-rays and γ -rays from the PWN are yielded by the same population of electrons/positrons which are injected into the nebula with a broken power-law spectrum. The X-rays are produced by the particles, which are freshly accelerated from the termination shock around the pulsar, with higher energies via synchrotron radiation, whereas the bulk of the GeV γ -rays are generated by the particles with rather lower energies compared with those producing the X-rays. As the particles with higher-energies diffuse outward in the nebula, their energies decrease gradually, and the γ -ray extension of the PWN is more extended than the X-ray one. As mentioned by H.E.S.S. Collaboration et al. (2012), the morphology in the VHE γ -rays shows no evidence of a distinct break in the populations of electrons, implying a continuous transition from older to younger electrons, which may not require a two-zone model for the SED of the PWN. For simplicity, as followed by previous work (H.E.S.S. Collaboration et al. 2012; Zhu et al. 2018; Joshi et al. 2023), we adopt a one-zone time-dependent leptonic model to describe the multi-wavelength SED.

For the electron spectrum, we assume a broken power-law with $\alpha_1 = 1.4$, $\alpha_2 = 2.5$ and $\gamma_b = 5 \times 10^6$, and the resulting SED of the PWN powered by PSR J1301-6305 at t_{age} is shown in Figure 6. The radio flux is 0.03 Jy at 4.85 GHz detected by the Parkes facility (Condon et al. 1993), which is set as an upper limit here due to the significance of the feature being only 3σ . The X-ray unabsorbed flux was determined to be $F = 1.6 \times 10^{-13} \text{ erg cm}^{-2} \text{ s}^{-1}$ in the 2–10 keV band (H.E.S.S. Collaboration et al. 2012). The magnetic field strength was fitted to be $B \sim 2.6 \mu\text{G}$ under the constraint of the X-ray flux. Such a low magnetic field strength is mainly due to the expansion of the PWN during the evolution. For instance, the magnetic field strength will decrease to about $3 \mu\text{G}$ for the Crab Nebula as it evolves in time to about 5000 yr (Torres et al. 2014). Here, the magnetic field strength of the nebula is relatively low due to its evolved large size. As affirmed in the left panel of Figure 5, at $t_{\text{age}} = 12,000 \text{ yr}$, the cooling time of the particles having a Lorentz factor $\gamma < 3 \times 10^8$ is primarily dominated by the adiabatic loss owing to the nebular expansion. With $\gamma > 3 \times 10^8$, synchrotron radiation becomes the dominant process for cooling particles, which leads to the softening of the particle spectrum with increasing energy, as can be seen in the right panel of Figure 5. The particle spectrum of the electrons/positrons with $\epsilon = 0.1$ at $t_{\text{age}} = 12,000 \text{ yr}$ has a break at γ_b and a cut-off $\gamma \sim 4 \times 10^8$ ($\sim 0.2 \text{ PeV}$). In Figure 6, the SED consists of a low-energy synchrotron radiation component and a high-energy one from the inverse Compton scattering off the soft photon fields, and the contribution of the

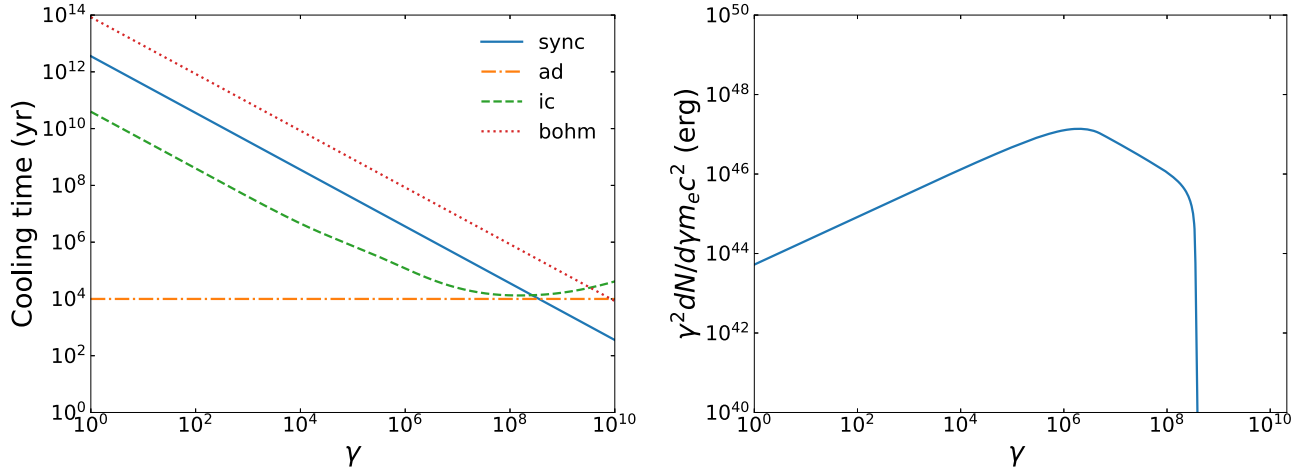


Figure 5. Left panel: Cooling times for synchrotron radiation, adiabatic loss, inverse Compton scattering and the escape time for Bohm diffusion at $t_{\text{age}} = 12,000$ yr. Right panel: The particle spectrum of electrons/positrons with $\epsilon = 0.1$ at $t_{\text{age}} = 12,000$ yr.

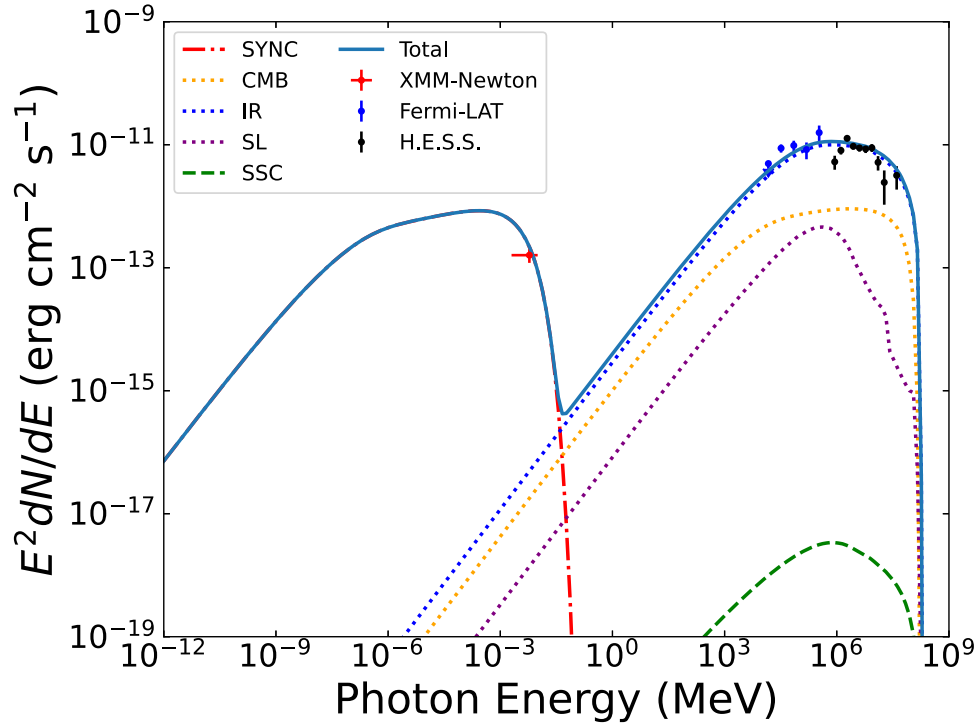


Figure 6. SED of HESS J1303-631. The red dot-dashed line represents synchrotron radiation, and the green, blue, orange and purple dotted lines are for inverse Compton scatterings off the synchrotron photons, IR, CMB and starlight, respectively. The total SED is displayed by the blue solid line. The observed fluxes in X-rays, TeV γ -rays (H.E.S.S. Collaboration et al. 2012) and GeV γ -rays with the Fermi-LAT (this work) are also shown in this figure.

synchrotron self-Compton process to the γ -rays can be neglected due to the relatively low magnetic field strength of $2.6 \mu\text{G}$. Using a broken power-law spectrum for the injected particles, the γ -ray fluxes can be well reproduced with the model.

5. Summary

In this paper, we give an analysis of the GeV γ -ray region coincident with HESS J1303-631 using about 14 yr of Fermi-LAT data. Previous analysis of the region using 45 months of Fermi-LAT data concluded that HESS J1303-631 is an

extended source characterized by a Gaussian with a dispersion of $0^\circ.45$ (Acero et al. 2013). This spatial range is found to contain the nearby SNR Kes 17, which may have some impact on the results. In this work, we ascertained that the best-fit extension of HESS J1303-631 is $R_{68} = 0^\circ.32 \pm 0^\circ.04$ with a TS value = 243.47 in the Gaussian template and photon flux of $(4.39 \pm 0.41) \times 10^{-10}$ ph cm $^{-2}$ s $^{-1}$ with a spectral index of 1.69 ± 0.09 in the 10–500 GeV energy band. Compared to the Fermi Galactic Extended Source catalog (Ackermann et al. 2017), which reported an extension of $0^\circ.33$ in a disk template with a spectral index of ~ 1.81 , we obtained a harder spectral index ($\Gamma \sim 1.69$). For comparison, we have shown the above mentioned and this work’s results in Figure 4. It is worth noting that HESS J1303-631 was recently reported in a PWN catalog (Eagle 2022), which consists of 11.5 yr of Fermi-LAT data. Eagle (2022) reported the best-fit extension $\sigma(^{\circ}) = 0.35$ with a radial Gaussian template in the 300 MeV–2 TeV energy band, and the spectral flux per bin for seven logarithmically spaced energy bins was obtained. Comparing the results, we obtained an extension radius $R_{68} = 0^\circ.32 \pm 0^\circ.04$ in the 10–500 GeV energy band, which is relatively consistent with the results given by Eagle (2022).

As indicated by Figure 1, the X-ray emission region is represented by the cyan contours. The X-ray emission from the PWN is dominated by the synchrotron radiation produced by high-energy leptons in the nebula, and the emission region is usually close to the pulsar, which is consistent with what is shown in Figure 1. HESS J1303-631 is a mature PWN of the pulsar PSR J1301-6305 (H.E.S.S. Collaboration et al. 2012). The morphological analysis indicates that the VHE emission region at low energies extends reasonably far from the pulsar toward the edge of the overall emission region, whereas the high-energy emission is more compact and closer to the pulsar. Furthermore, the GeV emission region exhibits an extension in the same direction as the TeV band.

Based on the one-zone time-dependent leptonic model for the SED of PWNe, the particles powered by PSR J1301-6305 with the broken power-law spectrum can produce the non-thermal emission by synchrotron radiation and inverse Compton scattering. The magnetic field strength is fitted to

be $\sim 2.6 \mu\text{G}$, which is a relatively low magnetic field and a reason for the missing radio observations of HESS J1303-631.

Acknowledgments

This work is supported by the National Natural Science Foundation of China (NSFC, grant Nos. U2031107 and 12063004), a grant from Yunnan Province (YNWR-QNBJ-2018-049), Yunnan Fundamental Research Projects (grant No. 202201BF070001-020), and the Program of Yunnan University (KC-22221102).

References

- Abdollahi, S., Acero, F., Ackermann, M., et al. 2020, *ApJS*, 247, 33
 Acero, F., Ackermann, M., Ajello, M., et al. 2013, *ApJ*, 773, 77
 Ackermann, M., Ajello, M., Baldini, L., et al. 2017, *ApJ*, 843, 139
 Aharonian, F., Akhperjanian, A. G., Aye, K.-M., et al. 2005, *A&A*, 439, 1013
 Akaike, H. 1974, *ITAC*, 19, 716
 Condon, J. J., Griffith, M. R., & Wright, A. E. 1993, *AJ*, 106, 1095
 Cordes, J. M., & Lazio, T. J. W. 2002, arXiv:astro-ph/0207156
 de Oña Wilhelmi, E., López-Coto, R., Amato, E., et al. 2022, *ApJL*, 930, L2
 Driessen, L. N., Domček, V., Vink, J., et al. 2018, *ApJ*, 860, 133
 Eagle, J. L. 2022, PhD thesis, Clemson University, South Carolina
 Fang, J., Wen, L., Yu, H., et al. 2020, *MNRAS*, 498, 4901
 Gaensler, B. M., & Slane, P. O. 2006, *ARA&A*, 44, 17
 H.E.S.S. Collaboration, Abramowski, A., & Acero, F. 2012, *A&A*, 548, A46
 Holler, M., Schöck, F. M., Eger, P., et al. 2012, *A&A*, 539, A24
 Joshi, J. C., Tanaka, S. J., Miranda, L. S., et al. 2023, *MNRAS*, 520, 5858
 Lande, J., Ackermann, M., Allafort, A., et al. 2012, *ApJ*, 756, 5
 Lhaaso Collaboration, Cao, Z., & Aharonian, F. 2021, *Sci*, 373, 425
 Li, J., Liu, R.-Y., de Oña Wilhelmi, E., et al. 2021, *ApJL*, 913, L33
 Liu, X., Guo, X., Xin, Y., et al. 2023, *ApJ*, 942, 105
 Manchester, R. N., Hobbs, G. B., Teoh, A., et al. 2005, *AJ*, 129, 1993
 Martín, J., Torres, D. F., & Rea, N. 2012, *MNRAS*, 427, 415
 Principe, G., Mitchell, A. M. W., Caroff, S., et al. 2020, *A&A*, 640, A76
 Reynolds, S. P., Pavlov, G. G., Kargaltsev, O., et al. 2017, *SSRv*, 207, 175
 Sushch, I., Oya, I., Schwanke, U., et al. 2017, *A&A*, 605, A115
 Tanaka, S. J., & Takahara, F. 2010, *ApJ*, 715, 1248
 Torres, D. F., Cillis, A., Martín, J., et al. 2014, *JHEAp*, 1, 31
 van der Swaluw, E. 2003, *A&A*, 404, 939
 van der Swaluw, E., Achterberg, A., Gallant, Y. A., et al. 2001, *A&A*, 380, 309
 Voisin, F. J., Rowell, G. P., Burton, M. G., et al. 2019, *PASA*, 36, e014
 Wood, M., Caputo, R., Charles, E., et al. 2017, in Proc. 35th ICRC (ICRC2017) 301 (Bexco, Busan: PoS), 824
 Wu, J. H. K., Wu, E. M. H., Hui, C. Y., et al. 2011, *ApJL*, 740, L12
 Xin, Y.-L., Liao, N.-H., Guo, X.-L., et al. 2018, *ApJ*, 867, 55
 Zhang, L., Chen, S. B., & Fang, J. 2008, *ApJ*, 676, 1210
 Zhu, B.-T., Zhang, L., & Fang, J. 2018, *A&A*, 609, A110